Cold rolling of amorphous/crystalline Ag73.2Cu17.1Zr9.7 composite

Cold rolling of amorphous/crystalline $Ag_{73.2}Cu_{17.1}Zr_{9.7}$ composite

Alberto Castellero[a,*], Danilo Lussana[a], Dario Ripamonti[b], Giuliano Angella[b], Marcello Baricco[a]

[a] Dipartimento di Chimica and NIS, Università di Torino, Torino, Italy

[b] Istituto per l'Energetica e le Interfasi, CNR-IENI, Milano, Italy

*corresponding author: Alberto Castellero, Tel: + 39 011 670 7097, Fax: + 39 011 670 7855

e-mail address: alberto.castellero@unito.it

Abstract

In this work, the effect of cold rolling on structure, microstructure and mechanical properties of rapidly solidified $Ag_{73.2}Cu_{17.1}Zr_{9.7}$ (at.%) amorphous/crystalline composite, containing 80 wt.% Ag, is studied. The as quenched composite is mainly characterized by small amorphous droplets, rich in Cu and Zr, uniformly dispersed in a Ag-rich f.c.c. matrix, as a consequence of the miscibility gap in the liquid. After cold rolling, no phase transformation is detected, whereas a microstructural refinement of the f.c.c. Ag-rich matrix is observed. No evidence of plastic deformation or fracture of the amorphous droplets embedded in the Ag-rich matrix is visible, suggesting that strain is mainly sustained by the crystalline matrix. Microhardness values of both as quenched and rolled ribbons range around 240 HVN, indicating that no significant strain hardening occurs. Experimental values for hardness are successfully fitted considering Orowan and load bearing models. The additional contribution from Hall-Petch effect in the crystalline matrix brings to an overestimation of the calculated values with respect to the experimental ones. Interparticle free distance is smaller than crystallites size, indicating that a fine dispersion of small hard amorphous droplets inhibits dislocation motion in the matrix more effectively than grain boundaries.

Keywords: Ag alloys; metal matrix composite; liquid miscibility gap; rapid solidification; strengthening effect

Introduction

Composites typically consist of a two phase system with a second phase dispersed in a matrix. The resulting properties are the synergic combination of those of the constituents [1-2]. On the one hand, in metallic matrix composites (MMCs), the soft and ductile matrix can be reinforced by dispersion of hard ceramic particles

(e.g. TiC, TiB_2, ZrB_2) [3-4]. On the other hand, in metallic glass composites, the hard and fragile amorphous matrix can be ductilized by dispersion of soft and ductile crystalline particles, allowing significant permanent deformation upon compression and tension [5].

Both in MMCs and metallic glass composites a strong and cohesive interfacial bonding between the two phases is needed [3, 6]. The composites properties depend on volume fraction, size, shape and distribution of the second phase [1-2, 6-9]. The combination of these parameters leads to a characteristic interparticle free distance, which defines the effect of the second phase on the plastic deformation of the matrix [1-2]. In MMCs, finely dispersed submicron sized hard particles effectively inhibit dislocation motion in the crystalline matrix [1-2]. In the case of metallic glasses composites, finely dispersed ductile crystalline particles confine the propagation of shear bands in the amorphous matrix and partially support the deformation by dislocation activity [10].

Examples of typical methods to produce composites are mechanical alloying, melt infiltration and direct solidification of the melt [1, 5, 11]. An alternative route for producing composites directly from the melt is represented by the exploitation of a miscibility gap in the liquid [12], such as in the case of free cutting leaded brasses, where small droplets of Pb are confined at the grain boundaries of brass as a consequence of the immiscibility in liquid Cu-Pb and Pb-Zn systems [13]. When both liquids have a good glass forming ability, amorphous/amorphous composite microstructures can be formed [14]. Conversely, amorphous/crystalline composites can be obtained if only one of the two liquids is a good glass former [15].

In the case of Ag-Cu system, it has been shown [16-18] that the addition of Zr stabilizes a miscibility gap in the liquid state that can lead to the formation an amorphous/crystalline composite upon solidification. Moreover, rapid solidification of silver rich Ag-Cu-Zr alloys, which fulfil the silver content (80 wt%) of commercial jewellery alloys, leads to deep undercooling of the melt and to the separation of two liquids, one Ag-rich and the other (Cu, Zr)- rich, which solidify as Ag-rich f.c.c. solid solution and (Cu, Zr)- rich amorphous alloy, respectively [19]. The composite obtained in this way is characterized by spherical amorphous droplets dispersed in the ductile crystalline matrix, leading to hardness values significantly higher than commercial Silver 800/1000 [19], suggesting an improved wear resistance of the surfaces.

The effect of crystalline particles embedded in an amorphous matrix on mechanical properties have been widely investigated [5], whereas the role of amorphous precipitates into a ductile crystalline matrix is still unexplored. Therefore, in this work, the attention is focused on $Ag_{73.2}Cu_{17.1}Zr_{9.7}$ (at.%) amorphous/crystalline composite, by studying the effect of cold rolling on the stability of the amorphous phase, the microstructure and structure of the crystalline matrix, and the mechanical properties of the composite.

Experimental

Master alloy ingots were prepared by arc melting the pure elements under Ar atmosphere. Each ingot was re-melted several times in order to obtain a good homogeneity. Rapidly solidified ribbons (about 40 μm thick) were obtained by planar flow casting using a wheel speed of 15 m/s in Ar atmosphere.

Ribbons were cold rolled by a twin roller apparatus to various levels of deformation. The elongation, ε, was determined by measuring the ribbon length before (l_0) and after (l) cold rolling. Characterization of the samples was performed before and after cold rolling.

A PANalytical X'Pert X-ray diffractometer (XRD) with Bragg-Brentano geometry and Cu K_α radiation was used for structural characterisation. Structural and microstructural information were obtained by means of Rietveld analysis [20] using Maud software [21].

Microstructures of the cross section of ribbons were observed with a Leica Stereoscan 410 scanning electron microscope (SEM) operating with a tungsten filament as an electron source. As quenched ribbons were etched with 20% NH_4OH, 20% H_2O_2 and 40% ethanol. Chemical composition was estimated by means of an energy dispersion spectroscopy (EDS) microprobe (Oxford Instruments)

The composition of the droplets in the ribbons was estimated with a combination of EDS and image analysis as described in Ref. [22]. An image analysis of the backscattered SEM images was performed with the Leica Application Suite V. 4.2.0 software, in order to evaluate size distribution and volume fraction of the amorphous particles.

SEM investigations at higher magnification were performed on TEM samples (thinned by ion milling) with a SU-70 microscope by Hitachi equipped with STEM detector and provided with a field emission Schottky electron source. Images were taken with an acceleration voltage of 15 kV.

Transmission electron microscopy (TEM) characterization was performed using a JEOL 3010 microscope operating at 300 kV.

Thermal stability of the as spun and cold rolled ribbons was characterised by differential scanning calorimetry using a Perkin Elmer Diamond DSC. Two runs upon heating were performed in order to separate reversible from irreversible events. In the following of the work, only DSC traces obtained after subtraction of the second run to the first one are presented. Heating rates of 5, 10, 20, 30, 40 and 80 K/min were employed in order to estimate the activation energy for the crystallisation of the amorphous phase with the Kissinger method.

Vickers microhardness of the as quenched and cold rolled ribbons was evaluated using a Buehler microhardness tester with a load of 25 gf and averaging up to 36 measurements on the ribbon wheel side for each sample. Hardness was evaluated after optical measurement of the indents diagonals.

Results and discussion

The backscattered electron SEM image of Fig. 1(a), related to the etched cross section of the as quenched ribbon, shows the typical microstructure due to the liquid/liquid phase separation, where bright particles are immersed in a dark etched matrix. The dispersed particles mainly show a spherical shape, with dimensions that progressively increase from the wheel side to the atmosphere side. The presence of small elongated particles is likely due to the shear deformation imposed by the rotating wheel to the liquid during solidification. Larger elongated plates can be randomly observed as a consequence of the agglomeration of the liquid.

EDS analysis indicates that the matrix has a composition around $Ag_{95}Cu_4Zr_1$ (at.%). In the case of the dispersed droplets and plates, a wider range of composition was estimated, $Ag_{13\text{-}18}Cu_{48\text{-}50}Zr_{34\text{-}37}$ (at. %) because of the higher uncertainty of the analysis. Backscattered images at higher magnification of a non etched as quenched ribbon, Fig. 1(b), reveal more in detail the microstructure. Large droplets (diameter around 1-2 µm), which appear dark because of the composition contrast in absence of chemical etching, are uniformly distributed in the bright matrix, while submicron droplets (0.1-0.2 µm) can be found at the boundaries of the grains in the matrix, where triple points are clearly marked. The inset of Fig. 1(b) shows even smaller droplets with diameters below 0.1 µm.

The bright field TEM image of the as quenched ribbon, Fig. 2(a), shows a 200 nm droplet immersed in the matrix. The corresponding SAD pattern (inset) shows the spots corresponding to a f.c.c. type structure, together with the typical halo of an amorphous phase, that can be associated to the matrix and the droplet, respectively.

As previously suggested by TEM, the XRD pattern (wheel side) of the as quenched ribbon, Fig. 3(a), confirms the presence of only one crystalline phase, with a f.c.c. type structure and a lattice parameter of 0.4077 nm. This phase ideally corresponds to a binary solid solution having composition $Ag_{97.4}Cu_{2.6}$ (at.%) [23, 24]. The slightly larger amount of Cu obtained by EDS with respect to the one estimated by XRD, can be justified by the presence of Zr in the solid solution, since these two elements have opposite effects on the lattice constant of Ag solid solutions [23-25].

Fig. 4(a) shows the DSC trace of the as quenched ribbon at a 40 K/min. The irreversible exothermic signal observed at $T_{on\text{-}set}$ = 484 °C and T_{peak} = 497 °C can be associated to the crystallization of the amorphous phase detected by TEM. The value of the activation energy for crystallization obtained by means of the Kissinger method (353 kJ/mol, see table 1) is in agreement with those reported in the literature for amorphous alloys with similar compositions [26].

After cold rolling the ribbons, the amorphous plates show the typical failure feature with shear offsets at about 45° with respect to the rolling direction [27], as shown by the SEM backscattered electron image of Fig. 1(c), related to the sample cold rolled at ε = 48 %. Conversely, the amorphous droplets do not show any sign of deformation or fracture after cold rolling, as shown in Fig. 1(d) for the sample deformed at ε = 71 %. In the former case, the load imposed during rolling is transmitted to the amorphous plate through the soft and ductile Ag-rich matrix, which acts as a transmitting medium, inducing shear and, subsequently, fracture of the amorphous phase [27]. In the latter case, the spherical shape of the amorphous droplets strongly reduces stress concentration at the interface between the crystalline matrix and amorphous particles, inhibiting the nucleation of shear bands in the amorphous phase. Furthermore, the bright strips shown in Fig. 1(d) behind the spherical amorphous particles suggest that the droplets flow in the soft and ductile Ag-rich matrix as a consequence of the rolling.

Bright field TEM images of the rolled ribbons are reported in Figs. 2(b-d). They show a high density of dislocations in the crystalline matrix, which tend to accumulate at the interface between the matrix and the amorphous particles, as shown in Fig. 2(b) and Fig. 2(d) for the ribbons rolled at ε = 14 % and ε = 71 %, respectively. Increasing the strain up to 71 %, dislocations tend to reorganize in subgrain structures, with size around 200 nm, as shown in Fig. 2(c) and Fig. 2(d). When the strain is increased from 14 % to 71 %, the corresponding SAD patterns, Fig. 2(b) and Fig. 2(c), show a progressive broadening of spots related to the f.c.c. structure of the Ag-rich solid solution, indicating an increased degree of strain in the crystalline lattice as a consequence of the deformation.

Accordingly, XRD patterns of ribbons rolled at different strain (Fig. 3) show a broadening of the peaks of the f.c.c. Ag-rich solid solution, which corresponds to a progressive increase of the microstrain and decrease of the coherent scattering domain size (crystallites size), as reported in table 1. The value of the lattice constant does not significantly vary as a function of strain, indicating that the composition of the crystalline matrix remains constant.

The DSC traces of the ribbons rolled at different level of strain show the same irreversible exothermic peak for the crystallization of amorphous phase observed in the case of the as quenched sample, as shown in Fig.

4 (b-e). The values of the onset temperature, peak temperature, activation energy and heat of crystallization do not significantly vary as a function of strain (Table 1), indicating that the amorphous phase is not affected by the rolling process.

From the image analysis of the SEM micrographs at different magnification, the size distribution of the bi-dimensional section amorphous spherical particles was calculated for the as quenched ribbon and those rolled at strains of 14 % and 71 % (Fig. 5). For all the samples, similar distributions were found, showing a marked peak around 50 nm. In all cases, less than 3 % of the population shows a diameter larger than 250 nm. The mean value for the diameter of the spherical amorphous particles (58-60 nm) and the amorphous fraction (15-16 %) are very similar before and after rolling (Table 1).

Fig. 6 shows that the hardness values of the ribbons rolled at different strains (filled circles) remain constant as a function of deformation. For comparison, the hardness values for an amorphous phase with similar composition [28] (filled triangle) and for a melt spun crystalline solid solution $Ag_{95}Cu_4Zr_1$ (at.%) (open diamond) are reported.

In the description of the mechanical properties of composites, different models are proposed [1, 2]. The simplest model is the rule of mixture, in which the hardness of the composite is given by

$$H_{composite} = H_{am}V_{am} + H_mV_m \quad (1)$$

where, in our case, H_{am} and H_m are the hardness of the amorphous and crystalline matrix phases, respectively, V_{am} and V_m are the volume fraction of the amorphous and crystalline phases, respectively. In this case, the application of the rule of mixture gives a value (dotted line in Fig. 6) which is lower than the experimental results, suggesting that such a simple model is not suitable for describing the mechanical behaviour of this composite.

In the case of metal matrix nanocomposites, the hardening of the matrix can be mainly explained by the dislocation bowing effect introduced by Orowan [29], as a consequence of the fine dispersion of small hard particles in the metal matrix. The most common equation is the one modified by Ashby [30]

$$\Delta\sigma_{Orowan} = M\frac{0.4Gb}{\pi\sqrt{1-\upsilon}}\frac{\ln(r/b)}{\lambda} \quad (2)$$

where $\Delta\sigma_{Orowan}$ is the increase of the yield strength due to the finely dispersed hard particle, M is the Taylor factor (~ 3 for f.c.c. metals like Ag), G is the shear modulus of the matrix (26000 MPa for Ag), υ is the Poisson's modulus of the matrix (0.3 for Ag), r is the average radius of the dispersed hard particles, b is the

Burger's vector ($b = a/\sqrt{2}$ for the [110] direction in f.c.c. metals, where *a* is the lattice constant of the unit cell) and λ is the interparticle free distance.

The interparticle free distance, λ, can be calculates as [31]

$$\lambda = r\sqrt{2/3}(1.25\sqrt{\pi/V} - 2) \quad (3)$$

where *r* and *V* are the average radius and the volume fraction of the dispersed hard particles, respectively.

An additional contribution to the hardening is given by the load bearing effect [32], which is given by

$$\Delta\sigma_{load-bearing} = 0.5\sigma_m V \quad (4)$$

for spherical particles, where σ_m is the yield strength of the matrix and *V* is again the volume fraction of the dispersed hard particles.

In the case of a grain refined matrix, further strengthening can be given by the Hall-Petch effect [33, 34], which is expressed as

$$\Delta\sigma_{H-P} = K_{H-P} / \sqrt{D} \quad (5)$$

where $K_{H\text{-}P}$ is the Hall Petch constant and *D* is the diameter of the grains in the matrix.

In our case, the strengthening due to the Orowan effect, calculated on the basis of Eq. (2) and Eq. (3), remains constant for the as quenched (194 MPa) and the rolled samples (195-200 MPa) since the values of *r*, *V* and λ do not significantly vary before and after rolling (Table 1). Only a moderate strengthening derives from the load bearing effect (10 MPa), independently of the imposed strain. Considering the grain refinement induced by cold rolling and $K_{H\text{-}P} \sim 0.04$ MPa $m^{1/2}$ [35], the Hall-Petch contribution to the yield strength increases from 36 MPa for the as quenched ribbon up to 61-77 MPa for the ribbons rolled at different strains.

The strengthening contributions in terms of yield strength, σ_y, were converted in hardening contributions in terms of Vickers hardness, *HV*, by considering a ratio $\sigma_y/HV \sim 2$ for pure silver on the basis of the data reported in Refs. [36, 37]. Therefore, the hardness of the composite was estimated by considering the linear sum of the various contributions

$$HV_{composite} = HV_{matrix} + \sum_i HV_i$$

where the index *i* considers the contributions given by the Orowan, load-bearing and Hall-Petch effects.

The calculated values were compared with the experimental ones, as shown in Fig. 6. On the one hand, when only the contributions from the Orowan and load-bearing effects are considered (dashed line in Fig. 6), the calculated values successfully fit the experimental ones. On the other hand, when also the contribution

due to the Hall-Petch effect is taken in account (line + open squares), the hardness calculated for the rolled samples slightly overestimate the experimental values.

This finding suggests that the different contributions cannot be indistinctly summed all together, irrespectively of the corresponding physical meaning. In this case, the interparticle free distance is almost one order of magnitude smaller than the average crystallites size for all cold rolled samples, indicating that the main barrier to the motion of dislocations is represented by the dispersed amorphous hard particles rather than the grain boundaries in the crystalline matrix.

Conclusions

In this work, the effect of cold rolling on microstructure, structure, thermal stability and mechanical properties of rapidly solidified $Ag_{73.2}Cu_{17.1}Zr_{9.7}$ amorphous/crystalline composites was investigated.

The microstructure of the as quenched ribbons mostly consists of amorphous droplets embedded in a f.c.c. Ag-rich matrix. More rarely, the amorphous phase is present in form of plates.

Even after rolling up to ε = 71 %, no phase transformation was detected both in the amorphous and crystalline phase. The X-ray diffraction peaks of the crystalline phase show a clear broadening when the strain is increased, indicating a progressive refinement of the microstructure.

The deformation mechanism depends on the shape of the amorphous phase. Amorphous droplets do not show any sign of deformation or fracture because of the reduced stress concentration at interface with the crystalline matrix. Conversely, amorphous plates show the typical failure feature with shear offsets at about 45° with respect the rolling direction, since the ductile Ag-rich matrix acts as a transmitting medium, which transfers the load to the amorphous phase inducing shear and, subsequently, fracture.

Hardness values of the ribbons remain constant around 240 HVN before and after rolling, suggesting that no significant strain hardening occurs.

The mechanical properties of the composite could be explained in terms of the hard particles strengthening effect, without a significant contribution of the grain boundaries to the inhibition of dislocation motion.

Acknowledgements

The authors acknowledge financial support by MIUR (PRIN 2008) and the contribution of O. Lambert (INP-Grenoble) to the experimental work.

References

[1] T.W. Clyne, P.J. Withers, An Introduction to Metal Matrix Composite Materials, Cambridge University Press, Cambridge, 1993.

[2] G.E.Dieter, Mechanical Metallurgy, 2nd edition, McGraw-Hill Inc., New York, 1976.

[3] A.R. Kennedy, A.E. Karantzalis, S.M. Wyatt, J. Mater. Sci. , 34 (1999) 933.

[4] L. Lu, M.O. Lai, Y. Su, H L. Teo, C.F. Feng, Scripta Mater., 45 (2001) 1017.

[5] C.A Schuh, T.C. Hufnagel, U. Ramamurty, Acta Mater. 55 (2007) 4067.

[6] F. Szuecs, C.P. Kim, W.L. Johnson, Acta Mater., 49 (2001) 1507.

[7] C.C. Hays, C.P. Kim, W.L. Johnson, Mater. Sci. Eng. A 304-306 (2001) 650.

[8] G.Y. Sun, G. Chen, C.T. Liu, G.L. Chen, Scripta Mater. 55 (2006) 375.

[9] A. Castellero, T. Baser, J. Das, P. Matteis, J. Eckert, L. Battezzati, M. Baricco, J. Alloys Compd. 509 (2011) S99.

[10] E. Pekarskaya, C.P. Kim, W.L. Johnson, J. Mater. Res. 9 (2001) 2513.

[11] C. Moelle, I.-R. Lu, A. Sagel, R.K. Wunderlich, J.H. Perepezko, H.-J. Fecht, Mater. Sci. Forum, 269-271 (1998) 47.

[12] I. Kaban, M. Ko¨hler, L. Ratke, R. Nowak, N. Sobczak, N. Mattern, J. Eckert , A. L. Greer, S. W. Sohn, D. H. Kim, J. Mater. Sci. 47 (2012) 8360.

[13] H. Okamoto, Phase Diagrams for Binary Alloys, ASM International, Materials Park (OH), 2000.

[14] A.A. Kündig, M. Ohnuma, D.H. Ping, T. Ohkubo, K. Hono, Acta Mater. 52 (2004) 2441.

[15] H.J. Chang, W. Yook, E.S. Park, J.S. Kyeong, D.H. Kim, Acta Mater. 58 (2010) 2483.

[16] A.A. Kündig, M. Ohnuma, T. Ohkubo, T. Abe, K. Hono, Scripta Mater. 55 (2006) 449.

[17] D.H. Kang, I.-H. Jung, Intermetallics 18 (2010) 815.

[18] D. Janovszky, K. Tomolya, A. Sycheva, G. Kaptay, J. Alloys Compd. 541 (2012) 353.

[19] A. Castellero, D.H. Kang, I.-H. Jung, G. Angella, M. Vedani, M. Baricco, J. Alloys Compd. 536 (2012) S148.

[20] R. A. Young, The Rietveld method, Oxford University Press, New York, 1993.

[21] L. Lutterotti, S. Matthies, H.-R. Wenk, Proceeding of the Twelfth International Conference on Textures of Materials (ICOTOM-12), 1 (1999) 1599.

[22] A. Castellero. G. Angella, M. Vedani, M. Baricco, J. Alloys Compd. (2012), http://dx.doi.org/10.1016/j.jallcom.2012.11.115

[23] “Pearson’s Handbook of Crystallographic Data for Intermetallic Phases (vol. 2)”, P. Villars and L.D. Calvert (Eds.), American Society for Metals, Metals Park (OH), 1985, p. 806.

[24] “A Handbook of Lattice Spacings and Structures of Metals and Alloys”, W.B. Pearson (Ed.), Pergamon Press, Oxford, 1964, pp. 278-279.

[25] Y.Y. Cui, T.L. Wang, K.P. Tai, B.X. Liu, J. Alloys Compd. 488 (2009) 223.

[26] K. K. Song, P. Gargarella, S. Pauly, G. Z. Ma, U. Kühn, J. Eckert, J. Appl. Phys. 112 (2012) 063503.

[27] P. Rizzi, A. Habib, A. Castellero, L. Battezzati, Intermetallics, 33 (2013), 38.

[28] W. Zhang, A. Inoue, J. Mater. Res. 21 (2006) 234.

[29] E. Orowan, Internal stress in metals and alloys, The Institute of Metals, London, 1948.

[30] M.F. Ashby in Oxide dispersion strengthening, G.S. Ansell, T.D. Cooper, F.V. Lenel (Eds.), Gordon and Breach, New York (NY), 1958, p. 143-205.

[31] J.W. Martin, Micromechanisms in particle hardened alloys, Cambridge University Press, Cambridge, 1980.

[32] V.C. Nardone, K.M. Prewo, Scripta Metall. 20 (1986) 43.

[33] E.O. Hall, Proc. Phys. Soc. Lond. B64 (1951) 747.

[34] N.J. Petch, J. Iron Steel Inst. 17 (1953) 25.

[35] H. Conrad, K. Jung, Mater. Sci Eng. A 391 (2005) 272.

[36] D. Lussana, A. Castellero, D. Ripamonti, G. Angella, M. Vedani, A. Zambon, M. Baricco, Int. J. Mat. Res. 103 (2012) 9.

[37] G. Angella, M. Baricco, P. Bassani, A. Castellero, R. Casati, Q. Ge, D. Lussana, M. Vedani, A. Zambon, Proceedings of "34° Convegno Nazionale A.I.M.” (on CD), November 7-9, 2012, Trento, Italy, paper 116.

TABLE CAPTIONS

Table 1.

Structural, microstructural and calorimetric parameters of the $Ag_{73.1}Cu_{17.2}Zr_{9.7}$ composite ribbons at different levels of strain.

FIGURE CAPTIONS

Fig. 1.

(a): SEM image (back scattered electron) of the cross section of the as quenched ribbon after chemical etching. (b): As quenched ribbon: SEM image (backscattered electron) of the TEM sample. (c): SEM image (back scattered electron) of the cross section of the cold rolled ribbon (ε = 48%) showing the fracture of a plate of the amorphous phase. (d): SEM image (backscattered electron) of the TEM sample showing the undeformed spherical particles of the amorphous phase after cold rolling (ε = 71%).

Fig. 2.

(a): bright field TEM image and SAD pattern (inset) of the as quenched ribbon. (b): bright field TEM image and SAD pattern (inset) after cold rolling at ε = 14 %. (c) and (d): bright field TEM images, (c) and (d), with SAD pattern, inset in (c), after cold rolling at ε = 71 %.

Fig. 3.

XRD patterns of the $Ag_{73.1}Cu_{17.2}Zr_{9.7}$ composite ribbons at different levels of strain: 0 % (a), 14 % (b), 33 % (c), 48 % (d) and 71 % (e).

Fig. 4.

DSC traces of the $Ag_{73.1}Cu_{17.2}Zr_{9.7}$ composite ribbons at different levels of strain: 0 % (a), 14 % (b), 33 % (c), 48 % (d) and 71 % (e).

Fig. 5.

Size distribution of the amorphous droplets in the ribbons before (ε = 0 %) and after rolling (ε = 14 % and ε = 71 %).

Fig. 6.

Experimental values of Vickers hardness for $Ag_{73.1}Cu_{17.2}Zr_{9.7}$ composite ribbons before and after cold rolling (filled circles), unrolled amorphous phase [26] (filled triangle) and as quenched $Ag_{95}Cu_4Zr_1$ crystalline matrix (open diamond). Calculated values of Vickers hardness according to rule mixture (dotted line), Orowan + load bearing effects (dashed line) and Orowan + load bearing + Hall-Petch effects (line + open squares) as a function of strain.

Table 1

Cold rolling strain, ε (%)	**0 (a.q.)**	**14**	**33**	**48**	**71**
Ag-rich matrix lattice constant, *a* (nm)	0.4077	0.4077	0.4081	0.4082	0.4083
Crystallites size, *D* (nm)	> 500	430	340	280	270
Lattice microstrain (%)	$8.8 \cdot 10^{-4}$	$23.1 \cdot 10^{-4}$	$29.4 \cdot 10^{-4}$	$28.8 \cdot 10^{-4}$	$30.0 \cdot 10^{-4}$
Onset temperature at 40 K/min, T_x (°C)	484	485	485	485	486
Peak temperature at 40 K/min, T_p (°C)	497	497	497	498	499
Crystallization heat, ΔH_x (J/g)	6.8 ± 0.6	7.0 ± 0.5	6.5 ± 0.9	6.8 ± 0.9	6.9 ± 0.5
Crystallization activation energy, E_a (kJ/mol)	353 ± 15	362 ± 9	348 ± 17	345 ± 21	340 ± 15
Amorphous particle diameter, *d* (nm)	60	59	-	-	58
Amorphous volume fraction (%)	15-16	15-16	-	-	15-16
Interparticle free distance, λ (nm)	60	59	-	-	58

Figure 1

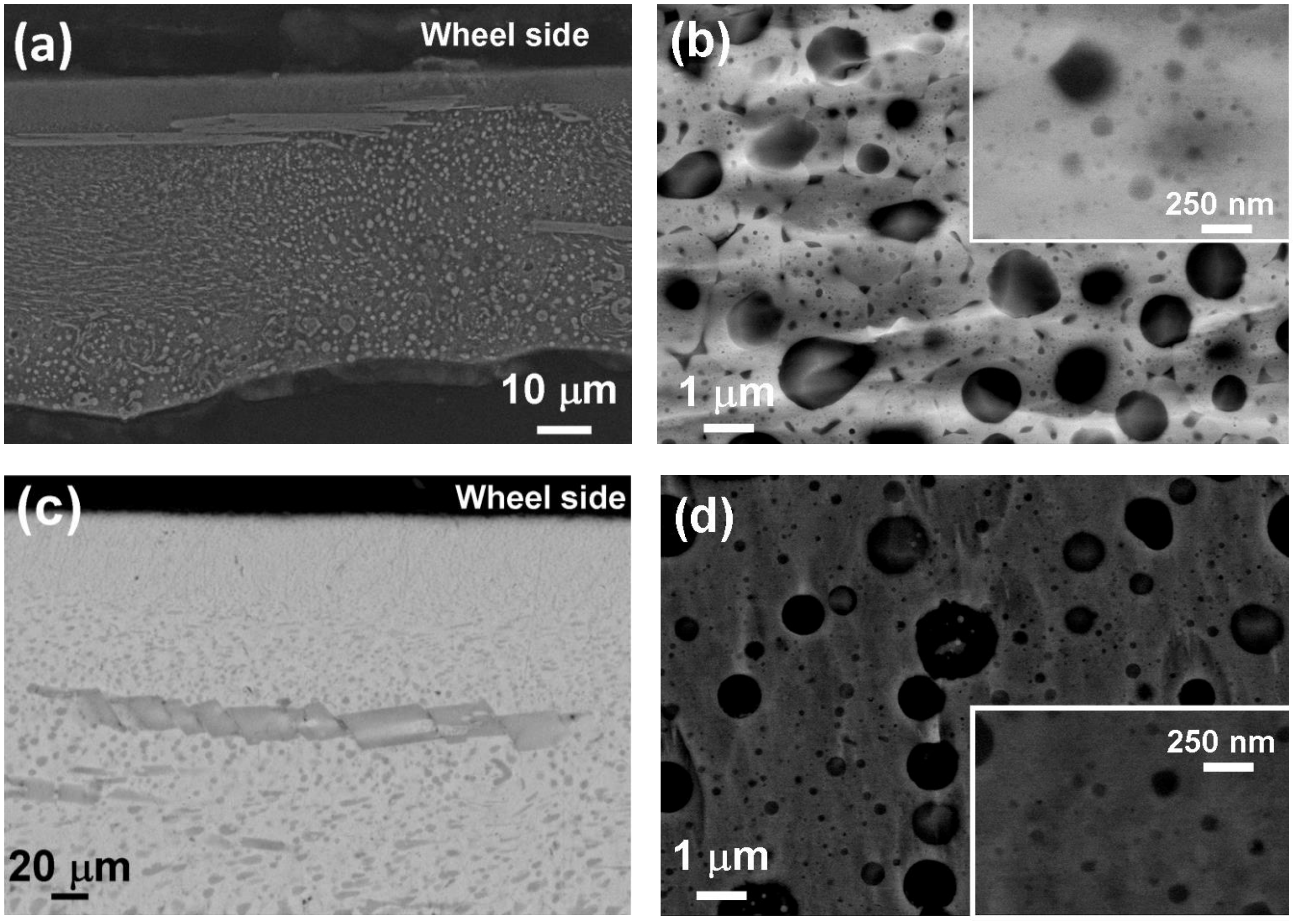

Figure 2

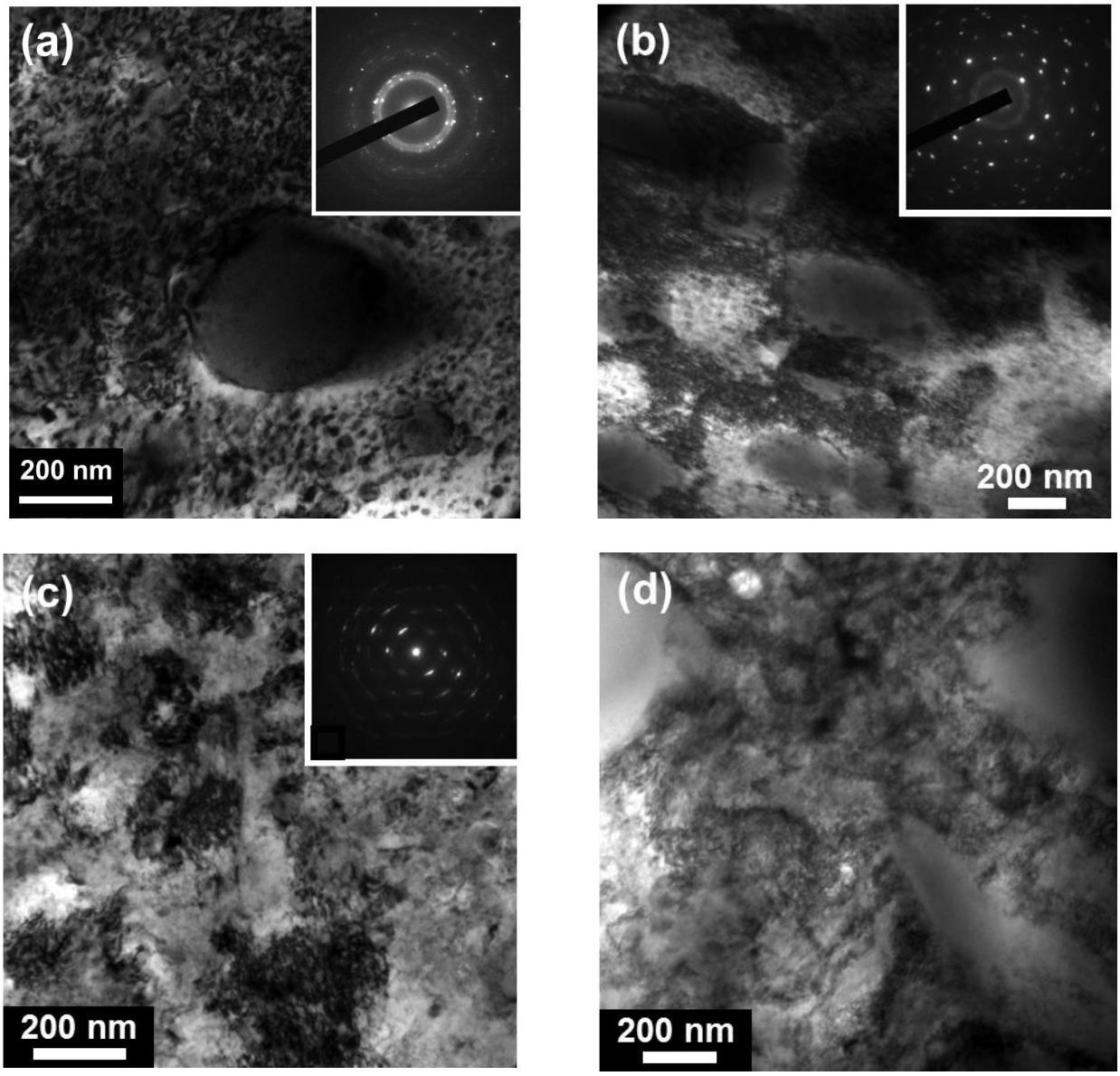

Figure 3

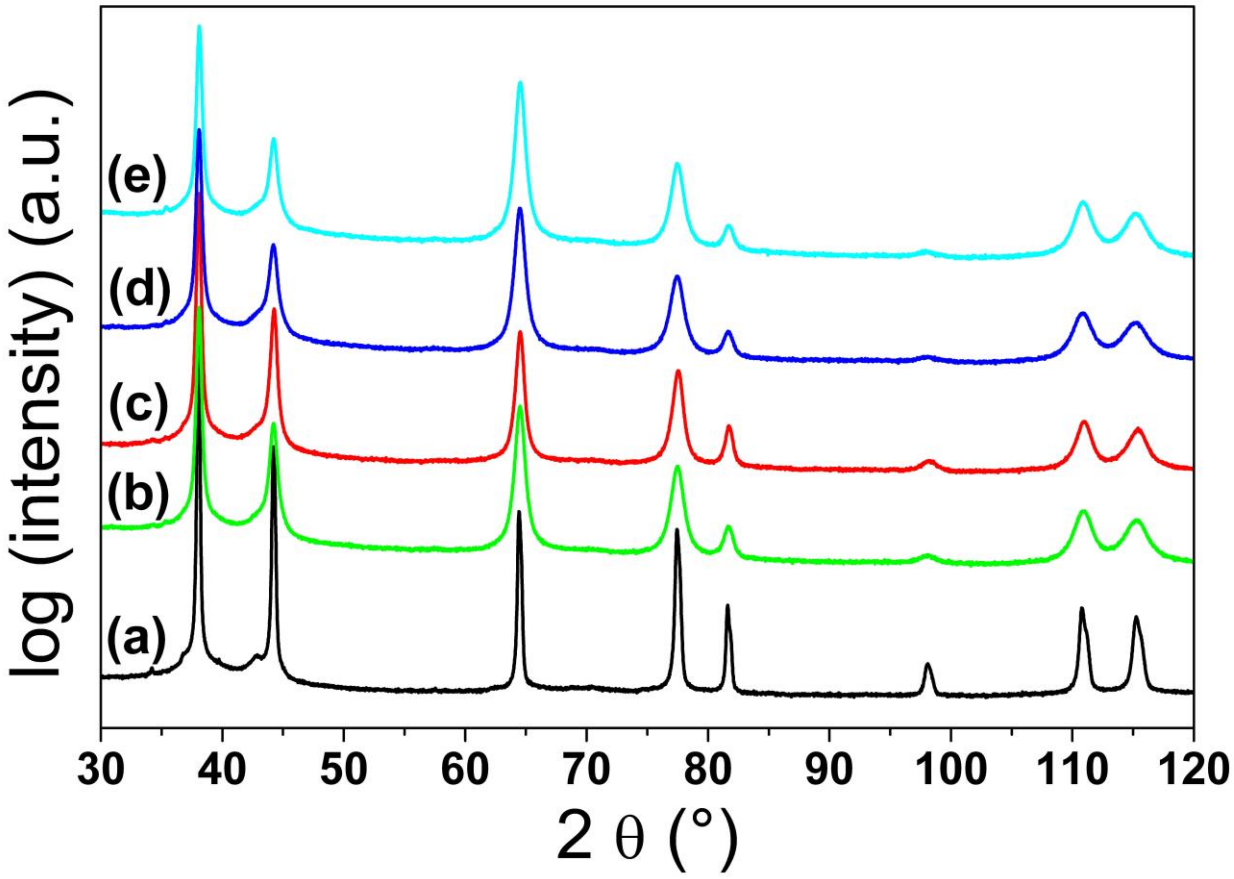

Figure 4

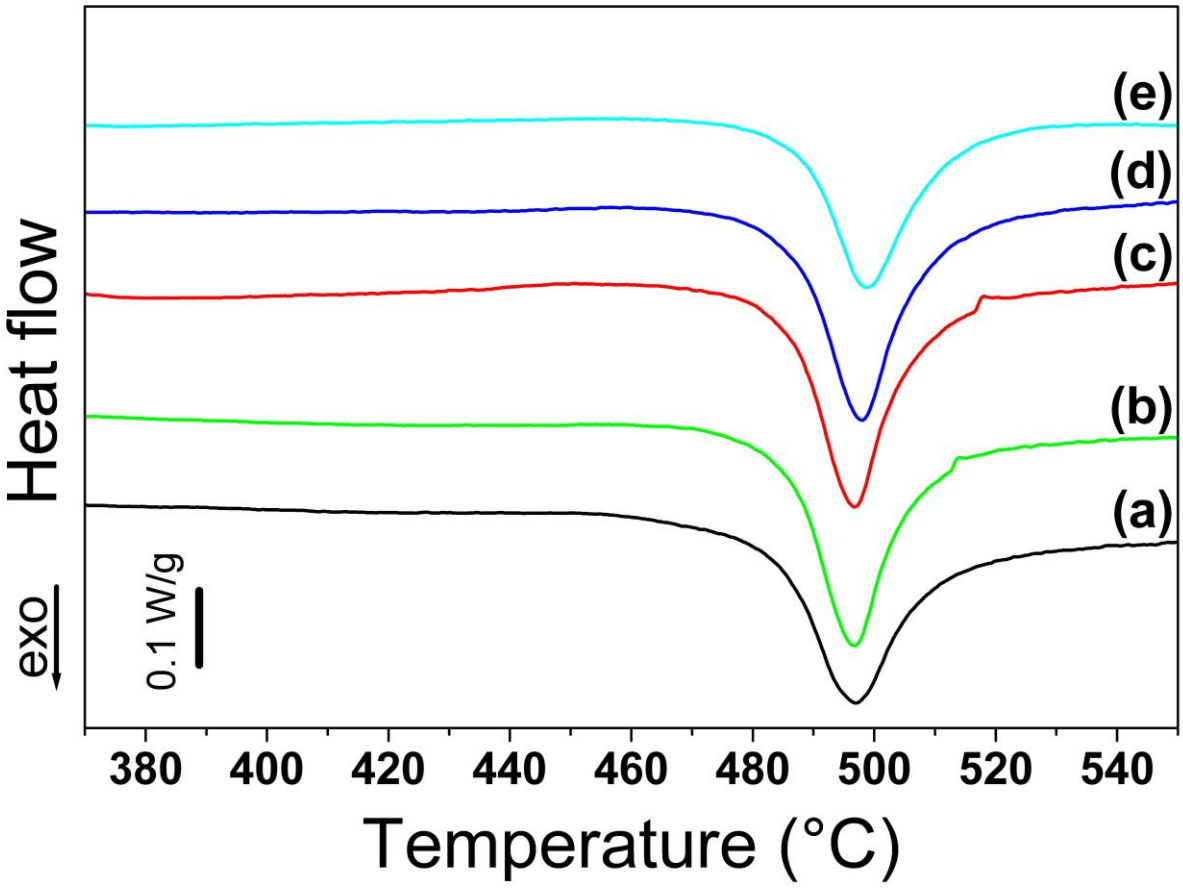
(e)
(d)
(c)
(b)
(a)
Heat flow
exo
0.1 W/g
380
400
420
440
460
480
500
520
540
Temperature (°C)

Figure 5

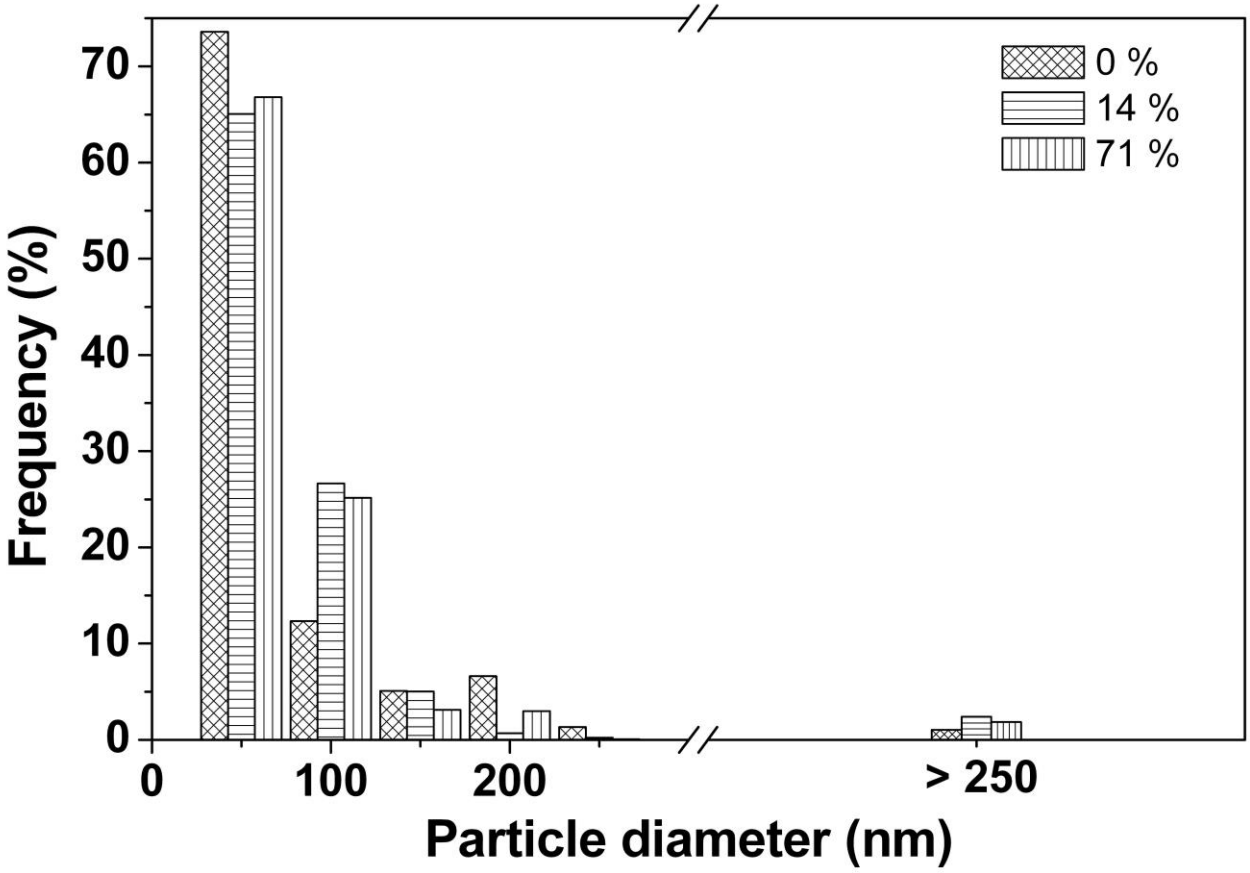
0 %
14 %
71 %
Frequency (%)
70
60
50
40
30
20
10
0
0
100
200
> 250
Particle diameter (nm)

Figure 6

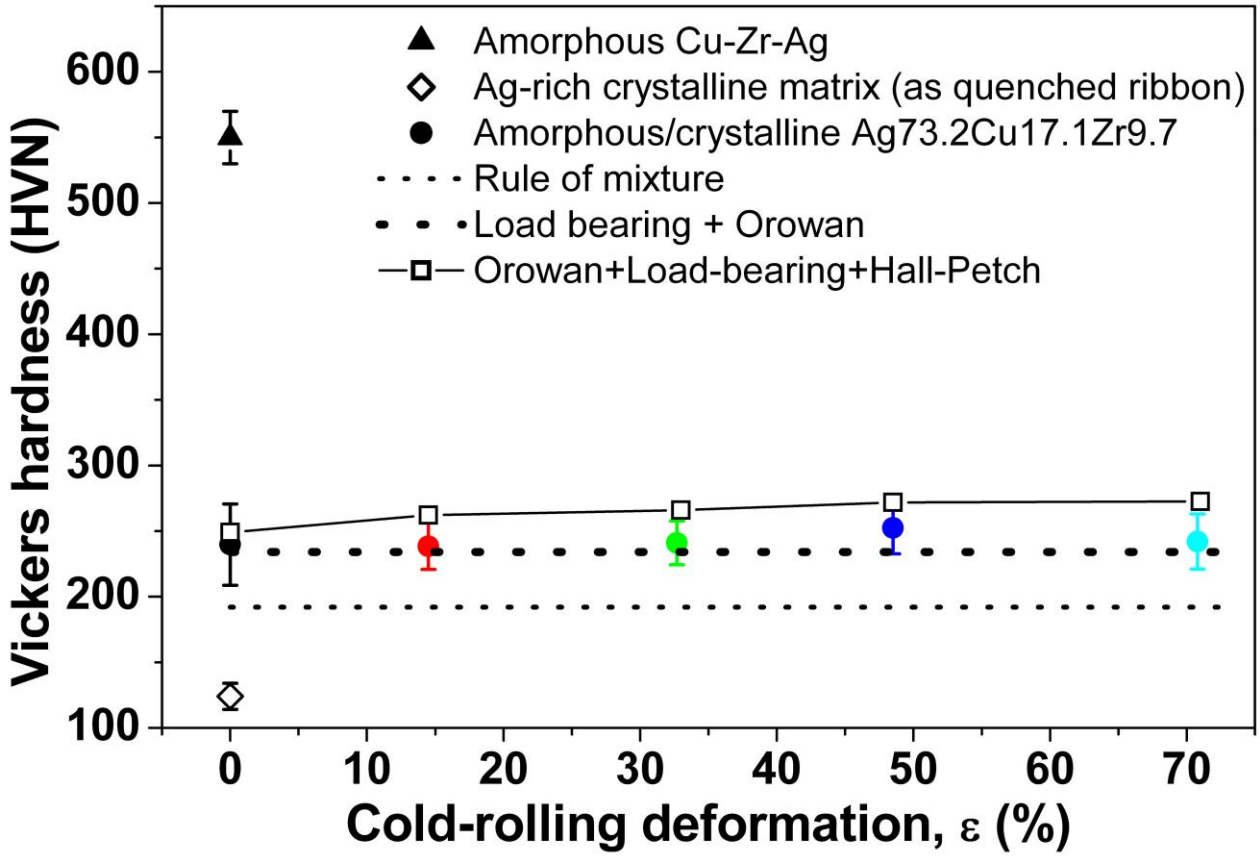
Amorphous Cu-Zr-Ag
Ag-rich crystalline matrix (as quenched ribbon)
Amorphous/crystalline Ag73.2Cu17.1Zr9.7
Rule of mixture
Load bearing + Orowan
Orowan+Load-bearing+Hall-Petch
Vickers hardness (HVN)
100
200
300
400
500
600
0
10
20
30
40
50
60
70
Cold-rolling deformation, ε (%)